IEEE Photonics Journal
An IEEE Photonics Society Publication

Open Access

High-Performance LSPR Fiber Sensor Based on Nanometal Rings

Volume 6, Number 2, April 2014

Yue Jing He

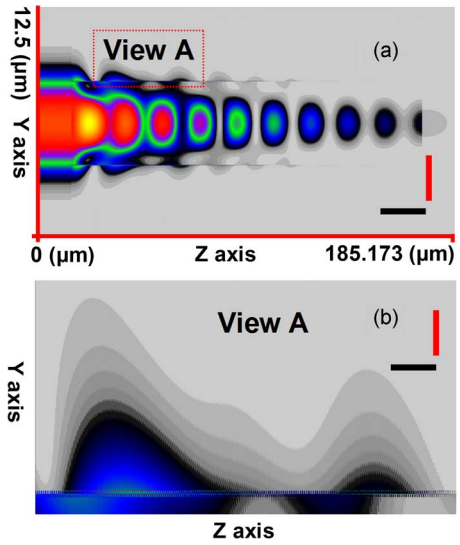

DOI: 10.1109/JPHOT.2014.2306828
1943-0655

High-Performance LSPR Fiber Sensor Based on Nanometal Rings

Yue Jing He

Department of Electronic Engineering, National Chin-Yi University of Technology, Taichung 41170, Taiwan

DOI: 10.1109/JPHOT.2014.2306828

Manuscript received January 15, 2014; revised February 6, 2014; accepted February 8, 2014. Date of publication February 19, 2014; date of current version March 24, 2014. This work was supported by the National Science Council of Taiwan under Grant NSC101-2622-E-007-CC3. Corresponding author: Y. J. He (e-mail: yuejing@ncut.edu.tw).

Abstract: A novel localized surface plasmon resonance (LSPR) fiber sensor was proposed. This LSPR fiber sensor was primarily constructed by conducting etching of the cladding layer and core layer on a single-mode fiber, followed by plating of 1444 nanometal rings. Sensor design and relevant calculations were conducted using a semi-analytical simulation method, which integrated the exact mode solver for the cylindrical coordinate and eigenmode expansion method. It was examined that the current metallic patterns in the fiber sensor can trigger the LSPR by the electric field E_r of the core mode HE_{11}, and this is the main reason why this novel fiber sensor can obtain high performance. After performing algorithms, images showed evident excitation of the LSPR. The LSPR fiber sensor designed in this paper possesses excellent attributes of short length (185.173 μm), high resolution (approximately -70 dB), and high sensitivity (approximately 34 257 nm/RIU).

Index Terms: Optical chemical LSPR fiber sensors, optical biological LSPR fiber sensors, eigenmode expansion method.

1. Introduction

In recent decades, several surface plasmon resonance (SPR) sensors adopting a fiber optic structure have been developed to reduce sensor size. These sensors provide highly sensitive and label-free biosensing for probing the affinity between biological molecules, and have been widely used in biology, biochemistry, and genetic engineering [1]–[16]. Recently, the excitation of surface plasmons in metal nanoparticles and their use in sensing applications has generated a lot of interest [17]–[31]. These are called localized surface plasmon resonance (LSPR) sensors. LSPR is another resonance phenomenon involving free electron waves in a metal, occurring in metallic nanostructures such as nanoparticles and nanometer-scale rough surfaces. In addition, at the THZ or GHZ frequency the refractive index of the metal is no longer related to the frequency and is considered a constant (the metal is considered a perfect electric conductor). It is called spoof-SPR and the electromagnetic waves, excluding radiation or diffraction, can only occur on metal surfaces in certain forms [32]–[38]. This study proposed a novel LSPR fiber sensor based on nano-metal rings. The side and cross-sectional structure diagrams of this sensor are shown in Figs. 1 and 2. Specifically, Segment (a) represents a general single mode fiber (SMF). Segment (b) illustrates the results of etching the cladding layer of Segment (a) and plating a metal material of a dm thickness. Segment (c) shows the structure formed by etching the entire cladding layer as well as the subsequent core layer by a thickness of d_m, followed by plating a metal material of a d_m thickness. The structural parameters of

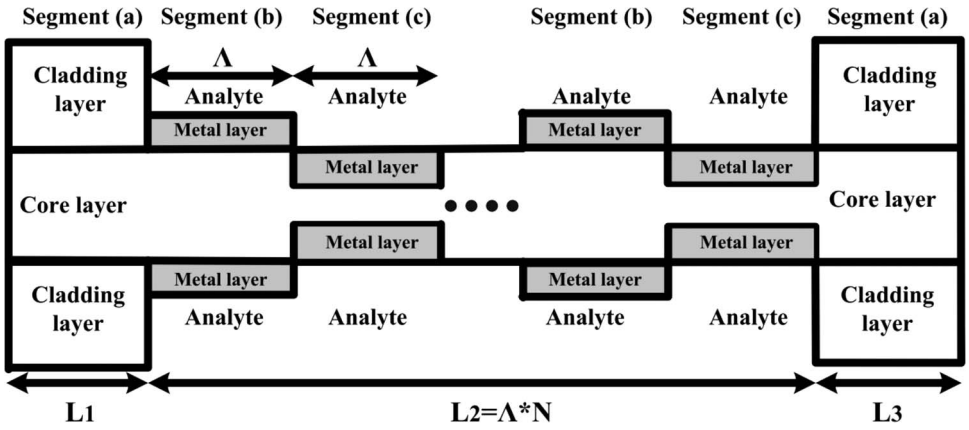

Fig. 1. LSPR fiber sensor side structure diagram.

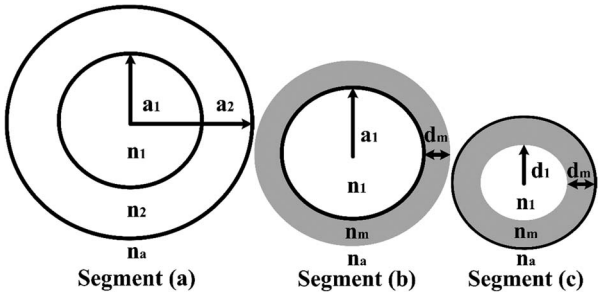

Fig. 2. LSPR fiber sensor cross-section structural diagram.

the sensor were set as follows: $a_1 = 2.25$ μm, $a_2 = 5.25$ μm, $d_1 = 2.23$ μm, $d_m = 0.02$ μm, $n_1 = 1.454$, $n_2 = 1.43$, $n_m = 0.56246309 + j9.840798407$ ($\lambda = 1550$ nm), $n_a = 1.33$, $\Lambda = 0.107461$ μm, $N = 1444$, $L_1 = 15$ μm, $L_2 = N * \Lambda = 155.173$ μm, and $L_3 = 15$ μm. The total length of the LSPR fiber sensor was $L = L_1 + L_2 + L_3 = 185.173$ μm. The total length of x axis (and that of y axis) used to simulated is 12.5 μm. The material used for the metallic layer in this study was gold. The complex refractive index of gold was obtained from the Handbook of Optical Constants of Solids (Academic Press, 1985) [39], and its precise wavelength-dependent fit to the data within was determined using a cubic spline algorithm, as shown in Fig. 1 of Reference 1.

LSPR fiber sensor is a very sensitive component for self-structure parameters, operating wavelength, and the variation of the refractive index of the analyte. Therefore, in the scope of LSPR fiber sensor, it is well-known that we have to understand beforehand the responses of LSPR fiber sensor for the above parameters before starting to construct LSPR fiber sensor actually. This study employed a semi-analytical technique that combines the exact mode solver for the cylindrical coordinate and eigenmode expansion method (EEM) in the LSPR fiber sensor design and simulation, and shows that by using this semi-analytical technique, the design and analysis of LSPR fiber sensor can be effortlessly accomplished by novice learners and application-level designers. In addition, the extensive use of graphics may help novice learners and application-level designers visually understand the transmission of optical signals in LSPR fiber sensor. Furthermore, the method introduced in the present study may be widely applied to component designs that have a periodic and cylindrical structure. It is also well-known that using the current technology for semiconductor fabrication, this novel LSPR fiber sensor proposed in this study can be easily realized [40]–[45].

The remainder of this paper is divided into the following sections: Section 2 provides a brief introduction to theories related to the exact mode solver for the cylindrical coordinate. For the three-layer cylindrical optical fiber, the exact electromagnetic fields and the dispersion relations of the

modes in the Segment (a), Segment (b), and Segment (c) were derived. After resolving the dispersion relations, the exact modes in the Segment (a), Segment (b), and Segment (c) can be obtained. The 2D power distribution of the core mode (HE_{11}) in the Segment (a) was plotted, enabling readers to understand the power distribution of the light source. After this novel LSPR fiber sensor was designed, the core mode HE_{11} was inputted into the left end of the sensor [the left end of Segment (a)] to demonstrate the physical phenomenon of power transmission in this novel sensor. Additionally, the 2D power distribution of the LSPR wave in the Segment (b) was plotted. It clearly explains that the current metallic patterns in the fiber sensor can trigger the LSPR by the electric field E_r of the core mode HE_{11}. Obviously, the main reason why this novel fiber sensor can obtain high performance is LSPR.

Section 3 introduces the theories related to the EEM. A detailed description is provided to explain how the EEM enables guided modes to conduct transmission in LSPR fiber sensor. However, this numerical method also has problems regarding accuracy. The Fourier series expansion is the main principle that enabled light wave transmissions to be performed using this numerical method. That is, if the number of modes was insufficient during the transfer process, even in non-absorbent media, the total power would decline as the number of implementing Fourier series expansion increased. We used the reverse thinking method to employ different numbers of guided modes to perform transmissions, consider the power lost, and determine the number of guided modes for this study. Here, we must emphasize that for non-absorbent media, the power lost in transmission distances is typically used to determine the sufficient mode quantity. However, that light wave power attenuates with distance in absorbent materials is a natural phenomenon. To determine the power loss caused by the Fourier series expansion, we should consider the original definition of loss. That is, observe the power loss conditions for every position of the Fourier series expansion execution. Because of the presence of gold and the absorbent material used in the structure for this study, when designing and analyzing the LSPR fiber sensor, we checked the power losses of all Fourier series expansion positions according to the basic definition of loss to verify the legitimacy of the eigenmode expansion method.

In Section 4, we summarize the content of Sections 2 and 3 to propose a rigorous, simple, and complete design process for analyzing and designing LSPR fiber sensor. Additionally, we employ numerous graphics to present the simulation results.

In the final section, we summarize the numerical simulation method used in this study, and use the data obtained in Section 4 to verify that the proposed novel LSPR fiber sensor possesses excellent attributes of short length (185.173 μm), high resolution (approximately -70 dB), and high sensitivity (approximately 34257 nm/RIU).

2. Exact Mode Solver

For the Segment (a), the exact electromagnetic fields in three layers can be written as follows [14]:

$$E_r = \left\{\frac{1}{r}C_1^a I_\ell(u_1^a r) - \frac{\beta_{\ell\nu}^a}{w\varepsilon_1}A_1^a u_1^a I'_\ell(u_1^a r)\right\}\sin(\ell\phi) \tag{1}$$

$$E_\phi = -\left\{C_1^a u_1^a I'_\ell(u_1^a r) - \frac{\beta_{\ell\nu}^a}{w\varepsilon_1}\frac{1}{r}A_1^a I_\ell(u_1^a r)\right\}\cos(\ell\phi) \tag{2}$$

$$E_z = \frac{u_1^{a^2}}{jw\varepsilon_1}A_1^a I_\ell(u_1^a r)\sin(\ell\phi) \tag{3}$$

$$H_r = \left\{-\frac{1}{r}A_1^a I_\ell(u_1^a r) + \frac{\beta_{\ell\nu}^a}{w\mu}C_1^a u_1^a I'_\ell(u_1^a r)\right\}\cos(\ell\phi) \tag{4}$$

$$H_\phi = -\left\{A_1^a u_1^a I'_\ell(u_1^a r) - \frac{\beta_{\ell\nu}^a}{w\mu}\frac{1}{r}C_1^a I_\ell(u_1^a r)\right\}\sin(\ell\phi) \tag{5}$$

$$H_z = -\frac{u_1^{a^2}}{jw\mu}C_1^a I_\ell(u_1^a r)\cos(\ell\phi) \tag{6}$$

inside the fiber core layer $(0 \le r \le a_1)$,

$$E_r = \left\{\frac{1}{r}\left[C_2^a I_\ell(u_2^a r) + D_2^a K_\ell(u_2^a r)\right] - \frac{\beta_{\ell\nu}^a}{w\varepsilon_2} u_2^a \left[A_2^a I_\ell'(u_2^a r) + B_2^a K_\ell'(u_2^a r)\right]\right\}\sin(\ell\phi) \tag{7}$$

$$E_\phi = -\left\{u_2^a\left[C_2^a I_\ell'(u_2^a r) + D_2^a K_\ell'(u_2^a r)\right] - \frac{\beta_{\ell\nu}^a}{w\varepsilon_2}\frac{1}{r}\left[A_2^a I_\ell(u_2^a r) + B_2^a K_\ell(u_2^a r)\right]\right\}\cos(\ell\phi) \tag{8}$$

$$E_z = \frac{u_2^{a^2}}{jw\varepsilon_2}\left[A_2^a I_\ell(u_2^a r) + B_2^a K_\ell(u_2^a r)\right]\sin(\ell\phi) \tag{9}$$

$$H_r = \left\{-\frac{1}{r}\left[A_2^a I_\ell(u_2^a r) + B_2^a K_\ell(u_2^a r)\right] + \frac{\beta_{\ell\nu}^a}{w\mu} u_2^a\left[C_2^a I_\ell'(u_2^a r) + D_2^a K_\ell'(u_2^a r)\right]\right\}\cos(\ell\phi) \tag{10}$$

$$H_\phi = -\left\{u_2^a\left[A_2^a I_\ell'(u_2^a r) + B_2^a K_\ell'(u_2^a r)\right] - \frac{\beta_{\ell\nu}^a}{w\mu}\frac{1}{r}\left[C_2^a I_\ell(u_2^a r) + D_2^a K_\ell(u_2^a r)\right]\right\}\sin(\ell\phi) \tag{11}$$

$$H_z = -\frac{u_2^{a^2}}{jw\mu}\left[C_2^a I_\ell(u_2^a r) + D_2^a K_\ell(u_2^a r)\right]\cos(\ell\phi) \tag{12}$$

inside the fiber cladding layer $(a_1 \le r \le a_2)$, and

$$E_r = \left\{\frac{1}{r} D_3^a K_\ell(w_3^a r) - \frac{\beta_{\ell\nu}^a}{w\varepsilon_3} B_3^a w_3^a K_\ell'(w_2^a r)\right\}\sin(\ell\phi) \tag{13}$$

$$E_\phi = -\left\{D_3^a w_3^a K_\ell'(w_3^a r) - \frac{\beta_{\ell\nu}^a}{w\varepsilon_3}\frac{1}{r} B_3^a K_\ell(w_3^a r)\right\}\cos(\ell\phi) \tag{14}$$

$$E_z = \frac{w_3^{a^2}}{jw\varepsilon_3} B_3^a K_\ell(w_3^a r)\sin(\ell\phi) \tag{15}$$

$$H_r = \left\{-\frac{1}{r} B_3^a K_\ell(w_3^a r) + \frac{\beta_{\ell\nu}^a}{w\mu} D_3^a w_3^a K_\ell'(w_3^a r)\right\}\cos(\ell\phi) \tag{16}$$

$$H_\phi = -\left\{B_3^a w_3^a K_\ell'(w_3^a r) - \frac{\beta_{\ell\nu}^a}{w\mu}\frac{1}{r} D_3^a K_\ell(w_3^a r)\right\}\sin(\ell\phi) \tag{17}$$

$$H_z = -\frac{w_3^{a^2}}{jw\mu} D_3^a K_\ell(w_3^a r)\cos(\ell\phi) \tag{18}$$

inside the analyte layer $(a_2 \le r)$. In Eqs. (1)–(18), A_1^a, C_1^a, A_2^a, B_2^a, C_2^a, D_2^a, B_3^a, D_3^a are field coefficients, and I_ℓ and K_ℓ are the modified Bessel function. After substituting the tangential fields into the boundary continuity conditions at the radii $r = a_1$ and $r = a_2$, as shown in Fig. 2, the exact and complex dispersion relation is given by

$$\zeta_a = \zeta_a'. \tag{19}$$

For the Segment (b), the exact electromagnetic fields in three layers and the complex dispersion relation can be written as Eqs. (1)–(19) with the field coefficients, A_1^b, C_1^b, A_2^b, B_2^b, C_2^b, D_2^b, B_3^b, and D_3^b. Similarly, for the Segment (c) the exact electromagnetic fields in three layers and the complex dispersion relation can be written as Eqs. (1)–(19) with the field coefficients, A_1^c, C_1^c, A_2^c, B_2^c, C_2^c, D_2^c, B_3^c, and D_3^c.

From Eq. (19), we can solve all the modes in three segments, with an operating wavelength of $\lambda = 1550$ nm. Because single-mode optical fibers were used, we obtained only one core mode, that is, HE_{11}, with an effective refractive index of n_{eff}^{core} $(n_2 < n_{eff}^{core} < n_1)$, and many numbers of cladding modes, with an effective refractive index of $n_{eff}^{cladding}$ $(n_a < n_{eff}^{cladding} < n_2)$. We initially obtained 35 guided modes comprising one core mode HE_{11}, as shown in Fig. 3, and 34 cladding modes (including LSPR wave).

According to the structural diagram of metal (Au) in LSPR fiber sensor (as shown in Fig. 4), in this manuscript the 2D power distribution of the first LSPR wave solved by the exact mode solver for the

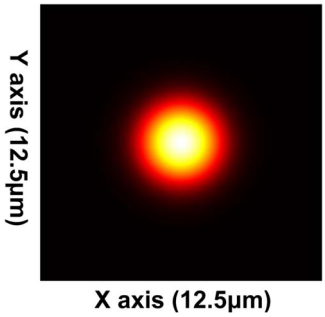

Fig. 3. The 2D power distribution of the core mode; the effective refractive index is $n_{eff}^{core} = 1.442631$. The total length of x axis (and that of y axis) used to simulated is 12.5 μm.

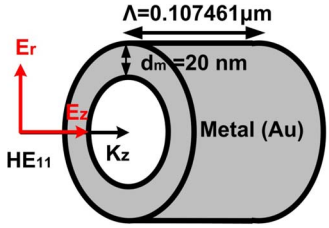

Fig. 4. The structural diagram of metal (Au) in LSPR fiber sensor.

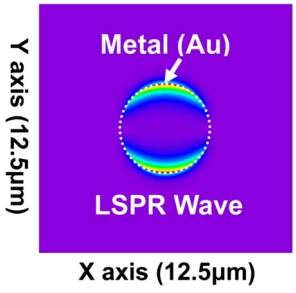

Fig. 5. The 2D power distribution of the first LSPR wave for the thickness of 20 nm (Au) on the r axis.

thickness of 20 nm (Au) on the r axis was shown in Fig. 5. Obviously, an analogous dipole is excited in this novel LSPR fiber sensor and it clearly explains that the current metallic patterns in the fiber sensor can trigger the LSPR by the electric field Er of the core mode HE_{11}. For the length $(\Lambda = 0.107461\ \mu m)$ on the z axis, the LSPRs triggered by the electric field E_z of the core mode HE_{11} is rather weaker than on the r axis. In other words, in this novel LSPR fiber sensor the physical phenomenon of LSPR excited for the waveguides, segment (b) and segment (c), is on the r axis and it dominates the LSPR of the waveguides [46], [47]. Obviously, LSPR triggered is the main reason why this novel fiber sensor can obtain high performance.

3. Eigenmode Expansion Method

The primary objective of the EEM was to prompt the guided mode to transmit power in the fiber structure. This study proposed a novel LSPR fiber sensor based on nano-metal rings. Side and cross-sectional diagrams of the sensor structure are presented as Figs. 1 and 2. Each segment object is considered a uniform waveguide that possesses a fixed refractive index value. The contact surface between segment object $k-1$ (Se_{k-1}) and segment object k (Se_k) is called junction $k-1$ (J_{k-1}). The modes that may exist in each segment object were recalculated. Next, power

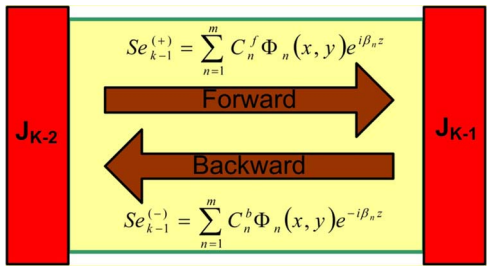

Fig. 6. Fourier series expansion for the forward and backward propagation modes.

conversions between segment objects were performed using the Fourier series expansion method. This method can also be employed to complete power transfers for the entire LSPR fiber sensor [1].

This indicates that the guided modes existing in the same segment of a periodic component are identical. Therefore, when using the exact mode solver to solve guided modes, only one segment must be calculated. This considerably reduces the computation time and memory required for the entire component simulation. In summation, combining the exact mode solver with the EEM is particularly suitable for designing periodic components which obtain cylindrical structure.

In each uniform waveguide (segment), the solution of the Maxwell equations is equivalent to Eq. (20), where the mode content Φ_n and propagation constant β_n are eigenfunctions and eigenvalues using the exact mode solver

$$E(x, y, z) = \Phi_n(x, y) e^{j\beta_n z}. \tag{20}$$

By combining Eq. (20) with the Fourier series expansion concept, and adding the entire forward propagation mode $\mathrm{Se}_k^{(+)}$, as shown in Eq. (21), and the back propagation mode $\mathrm{Se}_k^{(-)}$, as shown in Eq. (22), obtained using the exact mode solver, where $m = 35$ was the guided mode amount, and C_n^f and C_n^b were the coefficients for each forward and backward mode field, as shown in Fig. 6, the electric and magnetic fields within the uniform segment object Se_{k-1} can be obtained, as shown in Eqs. (23) and (24)

$$\mathrm{Se}_k^{(+)} = \sum_{n=1}^{m} C_n^f \Phi_n(x, y) e^{j\beta_n z} \tag{21}$$

$$\mathrm{Se}_k^{(-)} = \sum_{n=1}^{m} C_n^b \Phi_n(x, y) e^{-j\beta_n z} \tag{22}$$

$$\vec{E}(x, y, z) = \sum_{n=1}^{m} \left(C_n^f e^{j\beta_n z} + C_n^b e^{-j\beta_n z} \right) \vec{E}_n(x, y) \tag{23}$$

$$\vec{H}(x, y, z) = \sum_{n=1}^{m} \left(C_n^f e^{j\beta_n z} + C_n^b e^{-j\beta_n z} \right) \vec{H}_n(x, y). \tag{24}$$

After the propagated electromagnetic fields for a uniform segment object Se_{k-1} are obtained, power must be precisely transferred from segment object Se_{k-1} to segment object Se_k. Here, this study used the scattering matrix to transform the forward and backward power propagation of two adjacent segment objects, as shown in Eq. (25). In Fig. 7, $\mathrm{Se}_{k-1}^{(+)}$, $\mathrm{Se}_k^{(+)}$ and $\mathrm{Se}_{k-1}^{(-)}$, $\mathrm{Se}_k^{(-)}$ represent the total forward and backward propagation modes of the uniform segment objects Se_{k-1} and Se_k, and J_{k-1} represents the scattering matrix of the adjacent segment object junctions [1], [17]

$$\begin{bmatrix} \mathrm{Se}_{k-1}^{(-)} \\ \mathrm{Se}_k^{(+)} \end{bmatrix} = J_{k-1} \begin{bmatrix} \mathrm{Se}_{k-1}^{(+)} \\ \mathrm{Se}_k^{(-)} \end{bmatrix}. \tag{25}$$

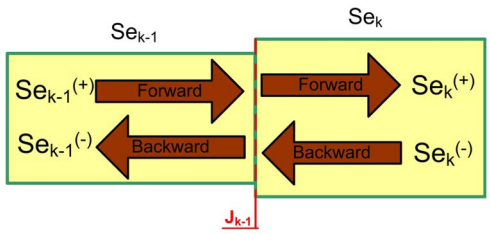

Fig. 7. The relationship between the field strength of the two adjacent uniform segment objects Se_{k-1} and Se_k.

To convert power between adjacent segment objects, we employed the Fourier series expansion to obtain the unknown junction scattering matrix J_{k-1}. Finally, the propagation effects of LSPR fiber sensor could be accurately conducted and completed by following the steps of this method. After considering detailed descriptions of the EEM, we can clearly determine that for periodic objects, only one segment object is required. Then, by calculating each junction scattering matrix J_{k-1}, we can complete the simulation of the period object's power transfer phenomenon.

According to the detailed description of the EEM, we determined that in Eqs. (21)–(24), m represents the number of guided modes and can critically affect the accuracy of the method. From a mathematical perspective, the Fourier series expansion must include all the guided modes that existed in the structure. However, this is impossible for numerical simulations because the time and memory required to perform such calculations are excessive and cannot be tolerated. However, if the number of modes is insufficient, some power loss will occur during each pass through the scattering matrix for the adjacent segment object junction. Therefore, for this study, we employed the reverse thinking method, and searched for the minimum m value that satisfied the requirement that the power loss value could not exceed 10^{-4} $(10 \cdot \log_{10}(10^{-4}) = -40$ dB$)$.

4. Design and Simulation

Summarizing the numerical simulation methods described in Sections 2 and 3, in this section we proposed a rigorous and simplistic design process to complete the analysis and design of LSPR fiber sensor. This mechanism essentially comprises the following five procedures: (a) solve for the guided modes using the exact mode solver; (b) use the EEM to perform an algorithm for power transmission; (c) test whether the power loss obtained using the EEM satisfies the less than 10^{-4} $(10 \cdot \log_{10}(10^{-4}) = -40$ dB$)$ specification; (d) calculate the resolution of the LSPR fiber sensor; and (e) calculate the sensitivity of the sensor. All numerical calculations in this study were conducted using 35 modes.

After the LSPR fiber sensor was designed based on the above parameters, the core mode (as shown in Fig. 3) was inputted in the left end of Fig. 1. The power transmission (Poynting vector P_Z) algorithm was then conducted using EEM, and the results are shown in Fig. 8(a). To further observe the newly structured LSPR, the View A region in Fig. 8(a) was magnified, as shown in Fig. 8(b), which clearly indicates the excitation of the LSPR. Certainly, the loss of all mode expansion positions must satisfy the requirement of less than 10^{-4} $(10 \cdot \log_{10}(10^{-4}) = -40$ dB$)$ for employing the 35 guided modes. The calculation results of the mode expansion positions and power loss really satisfy the requirement of the aforementioned specification. Resolution and sensitivity are two important indicators for evaluating the quality of any sensor. In this study, these indicators are presented in detail using the calculation results of the LSPR fiber sensor spectrum. As far as the actual spectrum measurement of the LSPR sensor is concerned, the instrument, OSA, is used most frequently. How can we recognize which one is the resonance dip of the LSPR sensor against the noise? Obviously, the meaning of the resolution used in LSPR sensor is the ability of recognizing the resonance dip of the LSPR sensor against the noise for OSA.

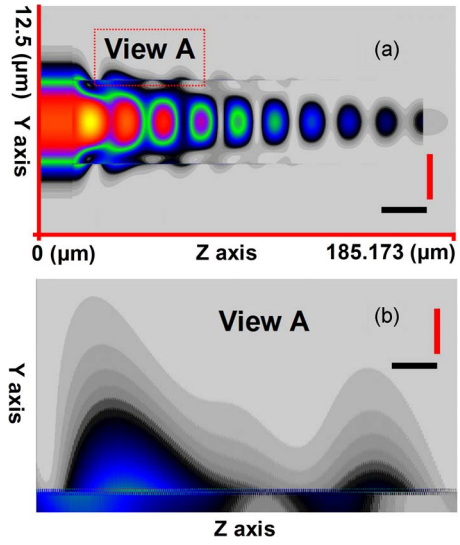

Fig. 8. (a) The Y-Z plane power transmission (Poynting Vector P_Z) of the core mode, and (b) A magnified image of the View A region in (a) with scale bar 7 and 26 μm for z axis and scale bar 36 and 145 μm for y axis.

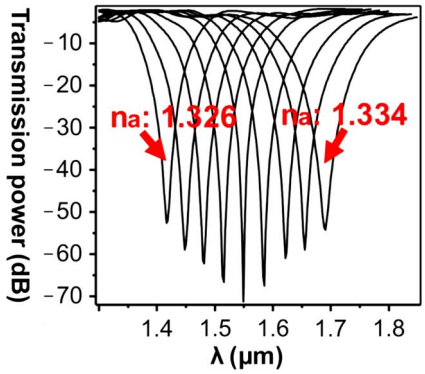

Fig. 9. Spectrum changes for the LSPR fiber sensor when the analyte refractive index n_a changed.

In addition, it is well-known that in the spectrum diagram the shift ability of resonance wavelength denotes the sensitivity of LSPR sensor when the refractive index of an analyte changes. To analyze the spectral characteristic of the LSPR fiber sensor, the bar transmission power is used as the following mathematical equation [1], [17]:

$$t_{=} = \frac{|R(z)|^2}{|R(0)|^2}. \tag{26}$$

Simply put, the bar transmission power is the self-power ratio of the incident core mode after traveling a certain distance (z) and when incidence occurs $(z = 0)$. Calculations for the core mode spectral patterns of various analytes using Eq. (26) are shown in Fig. 9. Specifically, the analyte refractive index changed from $n_a = 1.326$ to $n_a = 1.334$. An observation of Fig. 9 shows that this novel LSPR possesses a high resolution of approximately -70 dB at $\lambda = 1550$ nm. Fig. 10 indicates a diagram illustrating the relationship between resonance wavelength and the analyte refractive index in Fig. 9. From Fig. 10, the resonance wavelength of LSPR sensor shifted

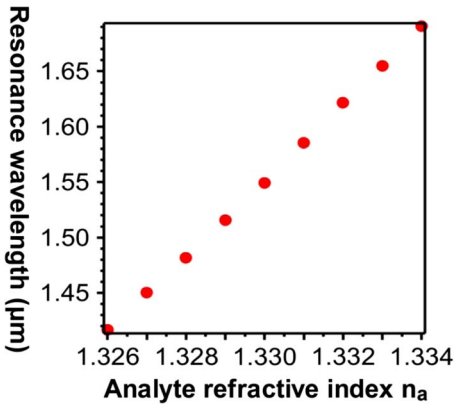

Fig. 10. The relationships between the analyte refractive index n_a and the LSPR's resonance wavelength.

from 1.4165625 μm to 1.690625 μm when the analyte refractive index changed from $n_a = 1.326$ to $n_a = 1.334$. Consequently, the sensitivity can be calculated as shown the following [1], [17]:

$$Sensitivity \approx \frac{(1.690625 - 1.4165625)}{(1.334 - 1.326)} \approx 34257\left(\frac{\text{nm}}{\text{RIU}}\right) \tag{27}$$

where RIU is refractive index unit. Comparing with the LPG-SPR fiber sensor which provides a length of approximately 1379.64571 μm, a resolution of approximately -45 dB, and a sensitivity of approximately 27000 nm/RIU [1], and the D-shape LSPR fiber sensor which provides a length of approximately 2494.4301 μm, a resolution of approximately -35 dB, and a sensitivity of approximately 20183.333 nm/RIU [17], Figs. 9 and 10 demonstrate that this novel LSPR fiber sensor possesses a short length of approximately 185.173 μm, a high resolution of approximately -70 dB, and a significantly high sensitivity of approximately 34257 nm/RIU.

5. Conclusion

A novel LSPR fiber sensor based on 1444 nano-metal rings was developed in this study. A semi-analytical simulation method integrating the exact mode solver for the cylindrical coordinate and EEM was employed to easily complete the design and analyses of the novel LSPR fiber sensor. According to the structural diagram of metal (Au) in LSPR fiber sensor, in this manuscript the 2D power distribution of the first LSPR wave was solved by the exact mode solver for the thickness of 20 nm (Au) on the r axis. Obviously, an analogous dipole is excited in this novel LSPR fiber sensor and it clearly explains that the current metallic patterns in the fiber sensor can trigger the LSPR by the electric field E_r of the core mode HE_{11}. In this novel LSPR fiber sensor the physical phenomenon of LSPR excited for the waveguides, segment(b) and segment(c), is on the r axis and it dominates the LSPR of the waveguides. Obviously, LSPR triggered is the main reason why this novel fiber sensor can obtain high performance. The simulation results facilitated in-depth observations of the LSPR; subsequently, a LSPR fiber sensor of short length (185.173 μm), high resolution (approximately -70 dB), and high sensitivity (approximately 34257 nm/RIU) was constructed.

References

[1] Y. J. He, "Investigation of LPG-SPR sensors using the finite element method and eigenmode expansion method," *Opt. Exp.*, vol. 21, no. 12, pp. 13 875–13 895, Jun. 2013.
[2] P. Bhatia and B. D. Gupta, "Surface-plasmon-resonance-based fiber-optic refractive index sensor: Sensitivity enhancement," *Appl. Opt.*, vol. 50, no. 14, pp. 2032–2036, May 2011.

[3] J. Cao, E. K. Galbraith, T. Sun, and K. T. V. Grattan, "Cross-comparison of surface plasmon resonance-based optical fiber sensors with different coating structures," *IEEE Sens. J.*, vol. 12, no. 7, pp. 2355–2361, Jul. 2012.
[4] X. Yu, S. Zhang, Y. Zhang, H. P. Ho, P. Shum, H. Liu, and D. Liu, "An efficient approach for investigating surface plasmon resonance in asymmetric optical fibers based on birefringence analysis," *Opt. Exp.*, vol. 18, no. 17, pp. 17 950–17 957, Aug. 2010.
[5] M. Gu, P. Bai, and E. P. Li, "Enhancing the reception of propagating surface plasmons using a nanoantenna," *IEEE Photon. Technol. Lett.*, vol. 22, no. 4, pp. 245–247, Feb. 2010.
[6] L. Y. Shao, Y. Shevchenko, and J. Albert, "Intrinsic temperature sensitivity of tilted fiber Bragg grating based surface plasmon resonance sensors," *Opt. Exp.*, vol. 18, no. 11, pp. 11 464–11 471, May 2010.
[7] K. H. An, M. Shtein, and K. P. Pipe, "Surface plasmon mediated energy transfer of electrically-pumped excitons," *Opt. Exp.*, vol. 18, no. 5, pp. 4041–4048, Feb. 2010.
[8] J. Wang, X. Chen, and W. Lu, "High-efficiency surface plasmon polariton source," *J. Opt. Soc. Amer. B*, vol. 26, pp. B139–B142, Nov. 2009.
[9] Y. S. Jung, J. Wuenschell, H. K. Kim, P. Kaur, and D. H. Waldeck, "Blue-shift of surface plasmon resonance in a metal nanoslit array structure," *Opt. Exp.*, vol. 17, no. 18, pp. 16 081–16 091, Aug. 2009.
[10] B. Špaèková and J. Homola, "Theoretical analysis of a fiber optic surface plasmon resonance sensor utilizing a Bragg grating," *Opt. Exp.*, vol. 17, no. 25, pp. 23 254–23 264, Dec. 2009.
[11] D. Choi, I. M. Lee, J. Jung, J. Park, J. H. Han, and B. Lee, "Metallic-grating-based interconnector between surface plasmon polariton waveguides," *J. Lightw. Technol.*, vol. 27, no. 24, pp. 5675–5680, Dec. 2009.
[12] Y. C. Lu, W. P. Huang, and S. S. Jian, "Influence of mode loss on the feasibility of grating-assisted optical fiber surface plasmon resonance refractive index sensor," *J. Lightw. Technol.*, vol. 27, no. 21, pp. 4804–4808, Nov. 2009.
[13] A. Wang, A. Docherty, B. T. Kuhlmey, F. M. Cox, and M. C. J. Large, "Side-hole fiber sensor based on surface plasmon resonance," *Opt. Lett.*, vol. 34, no. 24, pp. 3890–3892, Dec. 2009.
[14] Y. J. He, Y. L. Lo, and J. F. Huang, "Optical-fiber surface-plasmon-resonance sensor employing long-period fiber gratings in multiplexing," *J. Opt. Soc. Amer. B*, vol. 23, no. 5, pp. 801–811, Dec. 2006.
[15] G. Nemova and R. Kashyap, "Modeling of plasmon–polariton refractive-index hollow core fiber sensors assisted by a fiber Bragg grating," *J. Lightw. Technol.*, vol. 24, no. 10, pp. 3789–3796, Oct. 2006.
[16] Ó. Esteban, R. Alonso, M. C. Navarrete, and A. González-Cano, "Surface plasmon excitation in fiber-optics sensors: A novel theoretical approach," *J. Lightw. Technol.*, vol. 20, no. 3, pp. 448–453, Mar. 2002.
[17] Y. J. He, "Novel D-shape LSPR fiber sensor based on nano-metal strips," *Opt. Exp.*, vol. 21, no. 20, pp. 23 498–23 510, Oct. 2013.
[18] H. Y. Lin, C. H. Huang, G. L. Cheng, N. K. Chen, and H. C. Chui, "Tapered optical fiber sensor based on localized surface plasmon resonance," *Opt. Exp.*, vol. 20, no. 19, pp. 21 693–21 701, Sep. 2012.
[19] R. Dutta, R. Bharadwaj, S. Mukherji, and T. Kundu, "Study of localized surface-plasmon-resonance-based optical fiber sensor," *Appl. Opt.*, vol. 50, no. 25, pp. E138–E144, Aug. 2011.
[20] Y. Liu, Y. Zou, and R. G. Lindquist, "A reflection-based localized surface plasmon resonance fiber-optic probe for biochemical sensing," *Biomed. Opt. Exp.*, vol. 2, no. 3, pp. 478–484, Feb. 2011.
[21] C. Y. Tsai, S. P. Lu, J. W. Lin, and P. T. Lee, "High sensitivity plasmonic index sensor using slablike gold nanoring arrays," *Appl. Phys. Lett.*, vol. 98, no. 15, p. 153 108, Apr. 2011.
[22] S. K. Srivastava and B. D. Gupta, "Simulation of a localized surface-plasmon-resonance-based fiber optic temperature sensor," *J. Opt. Soc. Amer. A*, vol. 27, no. 7, pp. 1743–1749, Jun. 2010.
[23] R. Marty, G. Baffou, A. Arbouet, C. Girard, and R. Quidant, "Charge distribution induced inside complex plasmonic nanoparticles," *Opt. Exp.*, vol. 18, no. 3, pp. 3035–3044, Jan. 2010.
[24] M. J. Kofke, D. H. Waldeck, and G. C. Walker, "Composite nanoparticle nanoslit arrays: A novel platform for LSPR mediated subwavelength optical transmission," *Opt. Exp.*, vol. 18, no. 8, pp. 7705–7713, Mar. 2010.
[25] W. Y. Ma, H. Yang, J. P. Hilton, Q. Lin, J. Y. Liu, L. X. Huang, and J. Yao, "A numerical investigation of the effect of vertex geometry on localized surface plasmon resonance of nanostructure," *Opt. Exp.*, vol. 18, no. 2, pp. 843–853, Jan. 2010.
[26] V. V. R. Sai, T. Kundu, and S. Mukherji, "Novel U-bent fiber optic probe for localized surface plasmon resonance based biosensor," *Biosens. Bioelectron.*, vol. 24, no. 9, pp. 2804–2809, May 2009.
[27] H. Y. Lin, C. H. Huang, C. H. Chang, Y. Chiang Lan, and H. C. Chui, "Direct near-field optical imaging of plasmonic resonances in metal nanoparticle pairs," *Opt. Exp.*, vol. 18, no. 1, pp. 165–172, Dec. 2010.
[28] S. J. Yoon and D. Kim, "Target dependence of the sensitivity in periodic nanowire-based localized surface plasmon resonance biosensors," *J. Opt. Soc. Amer. A*, vol. 25, no. 3, pp. 725–735, Feb. 2008.
[29] S. K. Srivastava, R. K. Verma, and B. D. Gupta, "Theoretical modeling of a localized surface plasmon resonance based intensity modulated fiber optic refractive index sensor," *Appl. Opt.*, vol. 48, no. 19, pp. 3796–3802, Jun. 2009.
[30] D. F. G. Gallagher and T. P. Felici, "Eigenmode expansion methods for simulation of optical propagation in photonics—Pros and cons," *Proc. SPIE*, vol. 4987, pp. 69–82, 2003.
[31] M. Y. Ng and W. C. Liu, "Fluorescence enhancements of fiber-optic biosensor with metallic nanoparticles," *Opt. Exp.*, vol. 17, no. 7, pp. 5867–5878, Mar. 2009.
[32] C. R. Williams, S. R. Andrews, S. A. Maier, A. I. Fernández-Domínguez, L. Martín-Moreno, and F. J. García-Vidal, "Highly confined guiding of terahertz surface plasmon polaritons on structured metal surfaces," *Nature Photon.*, vol. 2, pp. 175–179, Feb. 2008.
[33] Q. Gan, Z. Fu, Y. J. Ding, and F. J. Bartoli, "Ultra-wide band slow light system based on THz plasmonic graded metal grating structures," *Phys. Rev. Lett.*, vol. 100, no. 25, p. 256 803, Jun. 2008.
[34] A. I. Fernández-Domínguez, L. Martín-Moreno, F. J. García-Vidal, S. R. Andrews, and S. A. Maier, "Spoof surface plasmon polariton modes propagating along periodically corrugated wires," *IEEE J. Sel. Topics Quantum Electron.*, vol. 16, no. 6, pp. 1515–1521, Dec. 2008.
[35] A. Rusina, M. Durach, and M. I. Stockman, "Theory of spoof plasmons in real metals," *Appl. Phys. A*, vol. 100, no. 2, pp. 375–378, Jun. 2010.

[36] S. A. Maier, S. R. Andrews, L. Martín-Moreno, and F. J. García-Vidal, "Terahertz surface plasmon polariton propagation and focusing on periodically corrugated metal wires," *Phys. Rev. Lett.*, vol. 97, no. 17, p. 176 805, Oct. 2006.
[37] J. J. Wu, H. E. Lin, T. J. Yang, Y. H. Kao, H. L. Chiueh, and D. J. Hou, "Open waveguide based on low frequency spoof surface plasmon polaritons," *J. Electromagn. Anal. Appl.*, vol. 5, no. 2, pp. 58–62, Feb. 2013.
[38] M. Navarro-Cía, M. Beruete, and S. Agrafiotis, "Broadband spoof plasmons and subwavelength electromagnetic energy confinement on ultrathin metafilms," *Opt. Exp.*, vol. 17, no. 20, pp. 18 184–18 195, Sep. 2009.
[39] E. D. Palik, *Handbook of Optical Constants of Solids*. Orlando, FL, USA: Academic, 1985.
[40] Y. C. Lin, W. H. Tsai, Y. C. Tsao, and J. K. Tai, "An enhanced optical multimode fiber sensor based on surface plasmon resonance with cascaded structure," *IEEE Photon. Technol. Lett.*, vol. 20, no. 15, pp. 1287–1289, Aug. 2008.
[41] V. P. Drachev, U. K. Chettiar, A. V. Kildishev, H. K. Yuan, W. Cai, and V. M. Shalaev, "The Ag dielectric function in plasmonic metamaterials," *Opt. Exp.*, vol. 16, no. 2, pp. 1186–1195, Jan. 2008.
[42] W. C. Chuang, A. C. Lee, C. K. Chao, and C. T. Ho, "Fabrication of optical filters based on polymer asymmetric Bragg couplers," *Opt. Exp.*, vol. 17, no. 20, pp. 18 003–18 013, Sep. 2009.
[43] K. M. Byun, S. J. Yoon, D. Kim, and S. J. Kim, "Experimental study of sensitivity enhancement in surface plasmon resonance biosensors by use of periodic metallic nanowires," *Opt. Lett.*, vol. 32, no. 13, pp. 1902–1904, Jun. 2007.
[44] K. Cottier, M. Wiki, G. Voirin, H. Gao, and R. E. Kunz, "Label-free highly sensitive detection of (small) molecules by wavelength interrogation of integrated optical chips," *Sens. Actuators B*, vol. 91, pp. 241–251, Jun. 2003.
[45] W. S. Weng, W. C. Chuang, I. F. Shyu, A. C. Lee, and C. T. Ho, "The fabrication of the Bragg grating on the D-shaped fiber," in *IEEE OptoElectron. Commun. Conf.*, Jul. 2009, pp. 1–2.
[46] J. Renger, "Excitation, interaction, and scattering of localized and propagating surface polaritons," Ph.D. dissertation, Technical Univ., Dresden, Germany, 2006.
[47] M. Hu, J. Y. Chen, Z. Y. Li, L. Au, G. V. Hartland, X. D. Li, M. Marquez, and Y. N. Xia, "Gold nanostructures: Engineering their plasmonic properties for biomedical applications," *Chem. Soc. Rev.*, vol. 35, no. 11, pp. 1084–1094, Sep. 2006.